Valve manoeuvre and wall shear stress characterization: numerical and experimental analyses

João Paulo Borges Coury Cavaleiro de Ferreira

Master Degree in Civil Engineering, Instituto Superior Técnico, University of Lisbon

Abstract: The current research aims at contributing to a better understanding in energy dissipation during hydraulic transients in pressurized pipes. A one-dimensional (1D) numerical model was developed based on the Method of Characteristics (MOC). The model incorporates the most relevant unsteady friction models developed in the past years and was calibrated and validated using experimental data collected from a facility installed at the Laboratory of Hydraulics and Environment, in the Department of Civil Engineering, Architecture and Geo-resources (DECivil) at Instituto Superior Técnico. The static and dynamic behaviour of the spherical valve located at the downstream end of the pipe was experimentally characterized to better describe this boundary condition in the numerical model. The valve head loss coefficients vary with the closure and with the flow regime for valve closure until 94% (i.e., 85° closure angle). The characterization of the dynamic valve behaviour allowed to determine the effective closure time of the valve as well as the closure curves laws, in order to numerically characterize the valve behaviour during transient events. Wall shear stress measurements were carried out using hot-film constant temperature anemometry technique during transient events. Results from a Computational Fluid Dynamics (CFD) model contributed to the discussion of the measurement uncertainties.

Keywords: Water hammer, 1D modelling, unsteady friction, spherical valve, wall shear stress, constant temperature anemometry.

1. Introduction

When industrial revolution began, urban areas were growing and water transport was becoming a major concern as water pipe systems provided safe water drinking and sanitation (Martins, 2016). With the higher complexity of hydraulic systems, hydraulic transient events turned into major concerns. Thus, transient events generated by valve manoeuvres, hydraulic turbo-machines start-up or stoppage, mechanical failures in surge protection devices or even sudden disruptions in the infrastructure started to be studied (Covas, 2003).

Nowadays, hydraulic transient events in pipes are commonly analysed using one-dimensional (1D) solvers for daily engineering purposes, since extreme pressures are well predicted (in the safe side). However, these models require an adequate characterization of the system components; the model will not describe properly the expectable real life events and accidents can occur due to improper design. Thus, the correct pipe system characterization must be defined and validated. Only afterwards can transient models be developed and simulations run. This becomes increasingly more important for the diagnosis of operational problems in existing systems.

One of the main differences between hydraulic transient events and the obtained results with 1D models, particularly in metal and concrete pipes (i.e., elastic pipes), is the energy dissipation due to the unsteady wall shear stress. This greatly affects the time that the system takes to restore another equilibrium configuration, as well as the amplitude, phase and shape of the pressure wave. Such issue is particularly relevant since the superposition of extreme pressures could compromise the system safety.

A well-managed operation is essential to cover energy, water and economical needs (Ramos *et al.*, 2000). In order to optimize operation procedures, each case must be independently analysed for the system worst case scenario (i.e. the one that compromises the system the most) and operational rules accordingly defined and/or new safety equipment specified (Ghidaoui and Zhao, 2005).

2. Background

2.1. Water hammer

One of the most important system characteristics for hydraulic transients analysis is the pressure wave celerity given by:

$$a = \sqrt{\frac{\frac{K}{\rho}}{1 + \frac{\alpha D}{e}\frac{K}{E}}} \tag{2.1}$$

in which D is the pipe inner diameter, K is the bulk modulus of elasticity of the fluid, ρ is the fluid density, e is the pipe wall thickness, E is the pipe Young's modulus of elasticity and α is a coefficient that depends on the axial constraints of the pipe.

For a pressure wave travelling along a pipeline between the device generating the transient and a reservoir, the wave period is given by:

$$T = \frac{4L}{a} \tag{2.2}$$

in which L is the total length of the pipe.

To obtain maximum transient pressures, Michaud (1878) developed a formula for *slow transient* events ($t_{ef} > 2L / a$):

$$\Delta H = \pm \frac{2LV_0}{g\, t_{ef}} \tag{2.3}$$

being ΔH the piezometric-head variation, V_0 the steady-state mean velocity, t_{ef} the effective closure time of the manoeuvre according to Lescovich (1967) and g the gravitational acceleration. Joukowsky (1900) developed a formula for *fast transients* ($t < 2L / a$):

$$\Delta H = \pm \frac{aV_0}{g} \tag{2.4}$$

During slow water hammer events, velocity profiles does not significantly vary. However, in fast transient events a vortex sheet is identified around the pipe inner surface (Martins *et al.*, 2016) and further dispersion increases energy dissipation. This phenomenon and major velocity gradients near the pipe wall explain the higher energy dissipation in fast transients.

Allievi (1902) developed, for the first time, the main water hammer equations, the system of partial differential equations, that is commonly solved using the Method of Characteristics (MOC):

$$\frac{a^2}{g}\frac{\partial V}{\partial x} + \frac{\partial H}{\partial t} = 0 \tag{2.5}$$

$$\frac{\partial V}{\partial t} + g\frac{\partial H}{\partial x} + \frac{4}{\rho D}\tau_w = 0 \tag{2.6}$$

being x the spatial coordinate, t the time coordinate, H the piezometric-head, V the mean velocity and τ_w the wall shear stress.

To ensure the MOC convergence and stability, the Courant-Friedrich-Lewy (CFL) condition must be satisfied, $Cr \leq 1$, being Cr the Courant number defined by the ratio between the real and the numerical wave celerity (Chaudhry, 2014):

$$Cr = \frac{a}{\frac{\Delta x}{\Delta t}} \tag{2.7}$$

being Δx and Δt the space and the time steps, respectively.

2.2. Friction models

The total wall shear stress has two main components, a steady and an unsteady that can be treated as independent:

$$\tau = \tau_{ws} + \tau_{wu} \tag{2.8}$$

in which τ_{ws} and τ_{wu} are the steady and the unsteady components of the wall shear stress, respectively.

The wall shear stress in steady-state flows is usually obtained by:

$$\tau_{ws} = \frac{1}{8} f \rho V \mid V \mid \tag{2.9}$$

where f , the friction factor, can be obtained by Hagen–Poiseuille formulation for laminar flows and by Darcy-Weisbach formulation for turbulent flows.

Several unsteady friction formulations have been developed, being the most relevant divided in two of the main common categories: i) instantaneous acceleration-based models (IAB) and ii) convolution-based models (CB). The former estimate wall shear stress based on the precious time step local and convective accelerations. The latter are based on the weighting average of past time velocity history.

The first major development on IAB models was Brunone *et al.* (1991) formulation, valid for turbulent flows:

$$\tau_{wu} = k_3 \frac{\rho D}{4}\left(\frac{\partial V}{\partial t} - a\frac{\partial V}{\partial x}\right) \tag{2.10}$$

in which k_3 is the decay coefficient.

Ramos *et al.* (2004) proposed an improvement of the previous formulation considering both the flow direction during transient events and two decay coefficients, one associated with wave shift, k_x , and the other with the pressure decay, k_t :

$$\tau_{wu} = \frac{\rho D}{4}\left(k_t \frac{\partial V}{\partial t} + k_x a\ \frac{|V|}{V}\frac{\partial V}{\partial x}\right) \tag{2.11}$$

The first CB model was proposed by Zielke (1968) who developed an analytical solution for laminar flows:

$$\tau_{wu}(t) = \frac{4\mu}{D}\int_0^t \frac{\partial V}{\partial t}(w) W(t-w) dw \tag{2.12}$$

where μ is the fluid viscosity, w is the integration constant and W is the weighting function to determine the weight of each past acceleration. The weighting function is described in terms of a non-dimensional time ($\Psi = 4t\nu / D^2$) by:

$$\begin{aligned} &W(\Psi) = 0.282095\Psi^{-1/2} - 1.25 + 1.057855\Psi^{1/2} \\ &+0.9375\Psi + 0.396696\Psi^{3/2} - 0.351563\Psi^2 \end{aligned} \tag{2.13}$$

for $\Psi < 0.02$ and

$$\begin{aligned} &W(\Psi) = e^{(-26.3744\Psi)} + e^{(-70.8493\Psi)} + \\ &e^{(-135.0198\Psi)} + e^{(-218.9216\Psi)} + e^{(-322.5544\Psi)} \end{aligned} \tag{2.14}$$

for $\Psi > 0.02$.

For turbulent flows, Vardy and Brown (2003) developed weighting functions according to the initial steady-state conditions:

$$W = \frac{\sqrt{(\nu_w\ /\ \nu_{lam})}\ e^{\left(-\Psi/C^*\right)}}{2\sqrt{\pi\Psi}} \tag{2.15}$$

in which ν_w is the kinematic viscosity at the wall ν_{lam} is the kinematic viscosity associated to laminar flow, Ψ is the non-dimensional time previously defined and C^* is a Reynolds dependent variable given by:

$$C^* = \frac{12.86}{\mathrm{Re}^{\kappa}} \therefore \kappa = \log_{10}\left(\frac{15.29}{\mathrm{Re}^{0.0567}}\right) \quad (2.16)$$

being Re Reynolds number and κ a Reynolds number dependent variable (Schlichting, 1979).

2.3. Wall shear stress measurement techniques

Shear measurements may be carried directly or indirectly. Direct measurements correspond to the measurement of the total amount of drag force experienced by a surface-mounted force balance (Berca, 2007). Indirect measurements are obtained through other physical or mechanical processes associated with the wall shear stress (e.g., unit energy dissipation in pipe for steady flow).

Direct measurement techniques comprehend floating element devices and oil-film interferometry. The former relies on the strain gauges deformation cause by the device movement for a certain flow rate. Oil-film interferometry is used by means of image processing while the oil near the pipe wall is dragged for a certain flow.

Indirect shear measurement techniques rely on other theories, such as heat-transfer theory, and some examples are hot-wire or hot-film interferometry. Three operation modes are distinguished in heat-transfer techniques: constant voltage anemometry (CVA), constant current anemometry (CCA) and constant temperature anemometry (CTA). Wall shear stress measurements have been also carried out using particle image velocimetry (PIV) by Brunone and Berni (2010) and Brito *et al.* (2014)

3. Experimental facility

The system consists of a 15.02 m copper pipe-rig with a 'reservoir-pipe-valve' configuration. The pipe has 1 mm of wall thickness, has a 105 GPa Young modulus of elasticity and is fixed each 0.60 m. A 60 l stainless steel hydropneumatic vessel is located at the upstream end simulating a constant head reservoir. For the carried out tests, this equipment was connected in derivation. Three pictures of the system are presented in Figure 1.

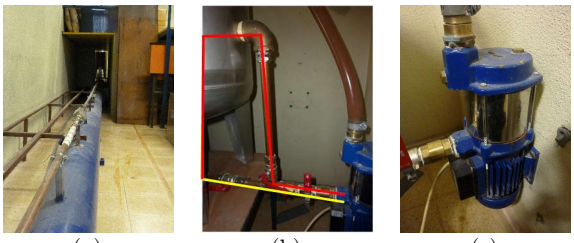

(a) (b) (c)

Figure 1. (a) Copper pipe; (b) hydropneumatic vessel operation modes (red – in-line; yellow – derivation); (c) pump

There are three valves at the downstream boundary: two identical spherical valves (V1 and V2) and a manual spherical valve (V3) to control the flow rate. Valve V1, which generates transient events, is pneumatically actuated valve, valve V2 is position controlled valve with the spherical valve positioner (SVP) attached. These valves are depicted in Figure 2.

(a) (b) (c)

Figure 2. Valves: (a) V1; (b) V2 and (c) V3

For pressure measurements, WIKA S-10 pressure transducers (PT) were used. Their nominal pressure is 25 bar and the accuracy span range is 0.25%, which corresponds to 0.30 m pressure error. Pressure measurements were carried out with a 40 kHz frequency. Initial flow rate was measured by a *Siemens MAG 1100* electromagnetic flow meter, which has an accuracy range of 0.4%. Low flow cut off occurs at 15 lh^{-1}.

A hot-film is installed at pipe mid-length to measure the wall shear stress and a MiniCTA is used to determine the heating need of the probe.

Four sets of tests have been carried out: Static tests for valve characterization; Dynamic tests for valve characterization (Tests D); Dynamic tests for model calibration and validation; Dynamic tests for wall shear stress measurement. The last two sets of tests were carried out for the same initial conditions as the static valve characterization. These were carried out for initial flow rates of 56.5 (laminar flow), 200 (transitional flow), 400 and 450 lh^{-1} (turbulent flows), resulting in Reynolds numbers of 999, 3536, 7073 and 7957, respectively.

4. Spherical valve behaviour

4.1. Valve static behaviour

With the obtained flow rate and pressure measurements and based on Eq.(4.1), head loss coefficients were obtained for each test S and closure angle:

$$K_V = 2gS_V^2 \frac{(H_u - H_d)}{Q^2} \quad (4.1)$$

Valve head loss coefficients, K_V, take the lowest values for the valve fully opened (0% closure); however, these K_V values vary with the initial flow conditions, being equal to 2, 7 and 20 for turbulent, transitional and laminar flows, respectively (Figure 3).

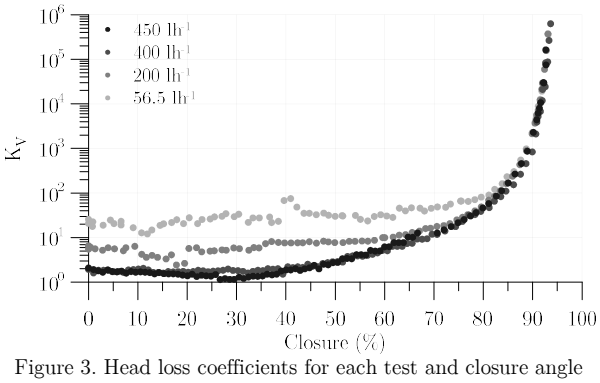

Figure 3. Head loss coefficients for each test and closure angle

These differences are due to two main reasons. The first is the higher uncertainties in pressure measurements for lower flow rates, as the measured head losses for laminar

flows (0.03-0.05 m) are lower than the accuracy range of the transducers (0.30 m); that occurs for a wide range of valve closure percentage. The second reason is the effect of viscous forces, which are dominant over inertial forces in laminar and transitional flows, leading to increased head losses in comparison with turbulent flows; these increased head losses are described by the higher K_V values for lower Re; this has also been supported by other researchers (White, 2010).

Experimental coefficients for the two turbulent flows are quite similar for the whole range of valve closure angles; these coefficients are associated with higher head losses and, consequently, with lower measurement uncertainties; in these tests, inertial forces and turbulence are also dominant over viscous forces.

Both transitional and laminar flow coefficients show higher discrepancies from the ones for turbulent flow, particularly from 0% until a 84% closure is reached, after which the values of K_V tend to overlap with those from turbulent flows. This is because, when the valve is almost closed, the flow is rapidly accelerated and highly turbulent inside the valve body; as such, flow conditions tend to be the same inside the valve independently of the initial flow regime; also, the pressure differences are much higher with less error associated.

4.2. Valve dynamic behaviour

To characterize the valve dynamic behaviour, first the closure time was analysed and two approaches were considered to describe the valve behaviour in the numerical model.

The total closure time, t_c, and effective closure time according to Lescovich (1967), t_{ef}, of the valve are presented in Table 1. For each initial flow rate, a combination of three closure times (controlled by the supplied air pressure, 2.5, 4.5 and 6.5 bars) have been tested. The valve closure time increases with the operating air pressure decrease in the valve control system. Despite the total closure time being significantly higher than the system characteristic time, $2L / a$ (0.024 s), all tests correspond to fast manoeuvres, since the effective closure times are significantly lower than $2L / a$, varying between 0.0028 and 0.0050s.

Table 1. Dynamic tests closure times

Test	Q_0 (lh^{-1})	Operating air pressure (bar)	Closure time, t_c (s)	Effective closure time, t_{ef}
D1	450	6.5	0.043	0.0028
D2		4.5	0.054	0.0031
D3		2.5	0.061	0.0046
D4	200	6.5	0.048	0.0016
D5		4.5	0.053	0.0023
D6		2.5	0.074	0.0032
D7	56.5	6.5	0.045	0.0020
D8		4.5	0.051	0.0044
D9		2.5	0.055	0.0050

For the characterization of the valve behaviour the two approaches considered are:

a) The *first approach* describes the discharge variation as an in-line valve, based on upstream and downstream pressure-head difference.

b) The *second approach* describes the discharge variation as a valve discharging to the atmosphere, considering only the upstream pressure-head measurement and assuming that the pressure-head at downstream is constant (in this case equal to the atmospheric pressure, null).

The *first approach* describes the valve discharge in transient conditions, Q, based on the pressure-head difference between both the upstream and downstream valve reaches, $H_u - H_d$, as an in-line valve installed in a pipe:

$$Q = C_d S_V \sqrt{2g\,(H_u - H_d)} \tag{4.2}$$

where C_d is the valve discharge coefficient, S_V is the totally opened valve cross-section area; and H_u and H_d are the piezometric-heads at upstream and downstream the valve, respectively. D1 to D3 tests final stages of closure are depicted in Figure 4.

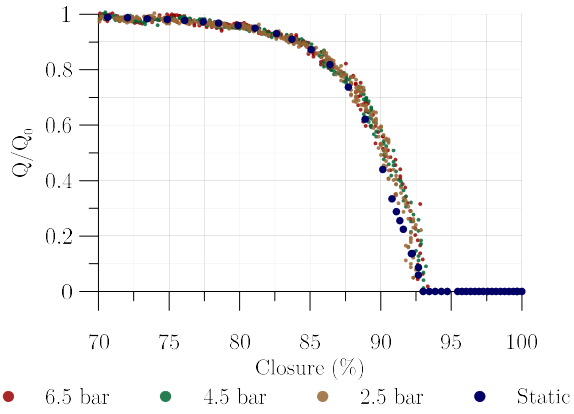

Figure 4. D1 to D3 dynamic valve behaviour tests first approach results

As expected, the valve dynamic behaviour follows almost the same valve law as for static conditions between 0% and 84% of closure. The valve is completely closed at 94% closure. This is observed for all initial discharges.

However, a small flow rate discrepancy is observed at the final stage of closure, between 84% closure and the total closure. For every initial flow rate, the higher the air pressure is, the faster the valve closes and the higher flow rate discrepancy becomes, leading to a steeper flow rate change at this stage (between 84% to 94% closure). This is because the faster the valve closes, the lesser time the flow has to reach an equilibrium, leading to a higher discrepancy from the static behaviour.

This valve closure approach is described by a hyperbolic function as:

$$\frac{Q}{Q_0} = 1 - \left(\frac{angle - m}{90}\right)^n \tag{4.3}$$

The constant parameters, m and n, that better fit experimental data, as well the coefficient of determination, R^2 , are presented in Table 2.

Table 2. Closure law coefficients for the first approach

First approach	m	n	R^2
D1	-6	24	0.99
D2	-6.13	24	0.99
D3	-6.25	24	0.99
D4	-5.2	31	0.97
D5	-5.35	31	0.97
D6	-5.5	31	0.96
D7	-3.15	55	0.91
D8	-3	55	0.91
D9	-2.75	55	0.95

The *second approach* describes the valve discharge in transient conditions, based the pressure-head at the upstream end, as if the valve was discharging to the atmosphere or to a constant head reservoir and the valve downstream pipe did not exist in the system. This flow rate variation is obtained by:

$$Q = Q_0 - \frac{gS\,(H_u - H_0\,)}{a} \tag{4.4}$$

in which H_0 is the initial head at the valve.

This is the common approach used in numerical models. This correspond to an artificial scheme in order to simplify the model, avoiding the numerical simulation of the return pipe at downstream the valve, but describing the valve as accurately as possible. Hence, a valve closure law is determined and modelled, neglecting the pressure downstream the boundary condition. The estimated flow rate variation for this second approach as if a discharge into atmosphere for D1 to D3 tests is depicted in Figure 5.

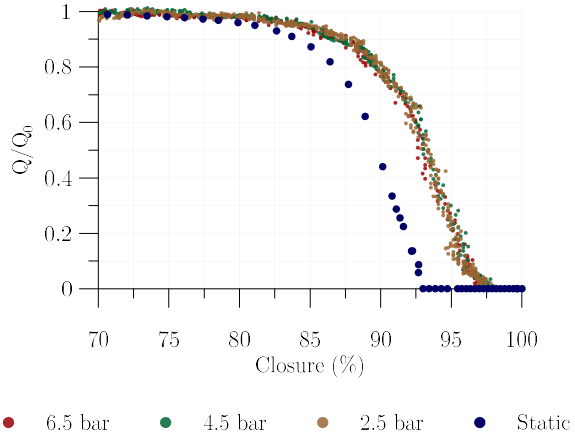

Figure 5. D1 to D3 dynamic valve behaviour tests second approach results

The valve discharge can be described by this approach as a sigmoid function:

$$\frac{Q}{Q_0} = \left(\frac{1}{1 + e^{-l(angle-m)}}\right)^n \tag{4.5}$$

where better-fitted constants are presented in Table 3.

Table 3. Closure law coefficients for the second approach

Second approach	l	m	n	R^2
D1	1.75	86	0.18	0.99
D2	1.75	86	0.19	0.99
D3	1.85	86	0.17	0.99
D4	1.5	86.5	0.3	0.99
D5	1.7	86	0.3	0.99
D6	4.2	86.5	0.1	0.98
D7	6	88.25	0.091	0.90
D8	6	88.5	0.08	0.91
D9	6	87.5	0.094	0.91

5. Numerical model

5.1. Model development

Using the mass and momentum equation, Eqs.(2.5) and (2.6), and using a rectangular characteristic grid (assuming that $V_0 \ll a$), the characteristic equations are obtained:

$$\begin{aligned} C^+ &: \frac{dQ}{dt} + \frac{gS}{a}\frac{dH}{dt} + RQ|Q| = 0 \\ C^- &: \frac{dQ}{dt} - \frac{gS}{a}\frac{dH}{dt} + RQ|Q| = 0 \end{aligned} \tag{5.1}$$

The resistance coefficient for laminar and turbulent flows are $R = 32\nu\,/\,(gD^2S)$ and $R = f\,/\,(2gDS^2)$, respectively. These equations are transformed into:

$$\begin{aligned} C^+ &: Q_{i,j} = C_P + C_{a+}H_{i,j} \\ C^- &: Q_{i,j} = C_N - C_{a-}H_{i,j} \end{aligned} \tag{5.2}$$

in which

$$C_P = \frac{Q_{i-1,j-1} + BH_{i-1,j-1} + C_{P1}{}' + C_{P1}{}''}{1 + C_{P2}{}' + C_{P2}{}''} \tag{5.3}$$

$$C_N = \frac{Q_{i+1,j-1} - BH_{i+1,j-1} + C_{N1}{}' + C_{N1}{}''}{1 + C_{N2}{}' + C_{N2}{}''} \tag{5.4}$$

$$C_{a+} = \frac{B}{1 + C_{P2}{}' + C_{P2}{}''} \tag{5.5}$$

$$C_{a-} = \frac{B}{1 + C_{N2}{}' + C_{N2}{}''} \tag{5.6}$$

in which $B = gS\,/\,a$ and subscripts i and j correspond to the space and time reaches, respectively.

C_{Pi} and C_{Ni} parameters with ' and '' superscripts refer to steady-state and unsteady-state friction components, respectively, as presented in Table 4.

Table 4. Numerical model coefficients

Steady-state friction		
Frictionless	$C_{P1}' = C_{P1}' = 0$ $C_{N1}' = C_{N1}' = 0$	
First-order accuracy	$C_{P1}' = -R^* \Delta t \lvert Q_{i-1,j-1} \rvert Q_{i-1,j-1}$ $C_{P2}' = 0$	$C_{N1}' = -R^* \Delta t \lvert Q_{i+1,j-1} \rvert Q_{i+1,j-1}$ $C_{N2}' = 0$
Second-order accuracy Chaudhry and Hussaini (1985)	$C_{P1}' = 0$ $C_{P2}' = R^* \Delta t \lvert Q_{i-1,j-1} \rvert$	$C_{N1}' = 0$ $C_{N2}' = R^* \Delta t \lvert Q_{i+1,j-1} \rvert$
Unsteady friction		
Brunone *et al.* (1991)	$C_{P1}'' = k_3\theta Q_{i,j-1} - k_3(1-\theta)(Q_{i-1,j-1} - Q_{i-1,j-2}) + k_3(Q_{i-1,j-1}) \lvert Q_{i,j-1} - Q_{i-1,j-1} \rvert$ $C_{N1}'' = k_3\theta Q_{i,j-1} - k_3(1-\theta)(Q_{i+1,j-1} - Q_{i+1,j-2}) + k_3(Q_{i+1,j-1}) \lvert Q_{i,j-1} - Q_{i+1,j-1} \rvert$ $C_{P2}'' = C_{N2}'' = k_3\theta$	
Bergant *et al.* (2001)	$C_{P1}'' = k_3\theta Q_{i,j-1} - k_3(1-\theta)(Q_{i-1,j-1} - Q_{i-1,j-2}) - k_3 SGN(Q_{i-1,j-1}) \lvert Q_{i,j-1} - Q_{i-1,j-1} \rvert$ $C_{N1}'' = k_3\theta Q_{i,j-1} - k_3(1-\theta)(Q_{i+1,j-1} - Q_{i+1,j-2}) - k_3 SGN(Q_{i+1,j-1}) \lvert Q_{i,j-1} - Q_{i+1,j-1} \rvert$ $C_{P2}'' = C_{N2}'' = k_3\theta$	
Ramos *et al.* (2004)	$C_{P1}'' = k_t\theta Q_{i,j-1} - k_t(1-\theta)(Q_{i-1,j-1} - Q_{i-1,j-2}) - k_x SGN(Q_{i-1,j-1}) \lvert Q_{i,j-1} - Q_{i-1,j-1} \rvert$ $C_{N1}'' = k_t\theta Q_{i,j-1} - k_t(1-\theta)(Q_{i+1,j-1} - Q_{i+1,j-2}) - k_x SGN(Q_{i+1,j-1}) \lvert Q_{i,j-1} - Q_{i+1,j-1} \rvert$ $C_{P2}'' = C_{N2}'' = k_t\theta$	
Trikha (1975) and Vardy *et al.* (1993)	$C_{P1}'' = C_{N1}'' = S\Delta t \frac{16\nu}{D^2} \sum_k \left[e^{-B_k \frac{4\nu}{D^2}\Delta t} Y_{k,j-1} - \frac{A_k}{S}(Q_{i,j} - Q_{i,j-1}) \right]$ $C_{P2}'' = C_{N2}'' = \Delta t \frac{16\nu}{D^2} \sum_k (A_k)$	
Zielke (1968) and Vardy and Brown (2003)	$C_{P1}'' = C_{N1}'' = \frac{16\nu}{D^2}\Delta t \cdot \left[W_{(t/\Delta t)} Q_{i,j-1} + \sum_{k=1}^{t/\Delta t - 1} W_{t/\Delta t-(k-1)} (Q_{i,k} - Q_{i,k-1}) \right]$ $C_{P2}'' = C_{N2}'' = \frac{16\nu}{D^2}\Delta t \cdot W_{(t/\Delta t)}$	

5.2. Model calibration

Celerity, steady-state friction and the valve manoeuvre must be calibrated in order to better describe the phenomenon in the tested system.

The celerity calibration was calculated by using the theoretical formula Eq.(2.1) and also based on the pressure wave period given by Eq.(2.2); the obtained results were 1269.2 and 1265.5 ms^{-1}, respectively. As both values are very close, the difference was considered negligible and the latter is considered onwards.

For steady-state friction calibration, friction factors were obtained for steady-state flows between 47.8 and 882.7 lh^{-1} experimentally and theoretically. A large difference was identified in the first measurements but this decreases as pressure measurements stand out of the pressure transducers span accuracy. As flow-rate increases, the difference becomes smaller and tends to Blasius formulation (smooth turbulent flows).

The valve closure laws presented in the spherical valve dynamic behaviour were tested in the numerical model and the one that gave better results was the law which only considered the upstream pressure for determining the flow rate variation (second approach). This is due to the lack of knowledge by the model of the flow conditions downstream the valve as the remaining system (returning hose and discharge into the upstream reservoir) was not modelled. Pressure wave results for each approach are depicted in Figure 6.

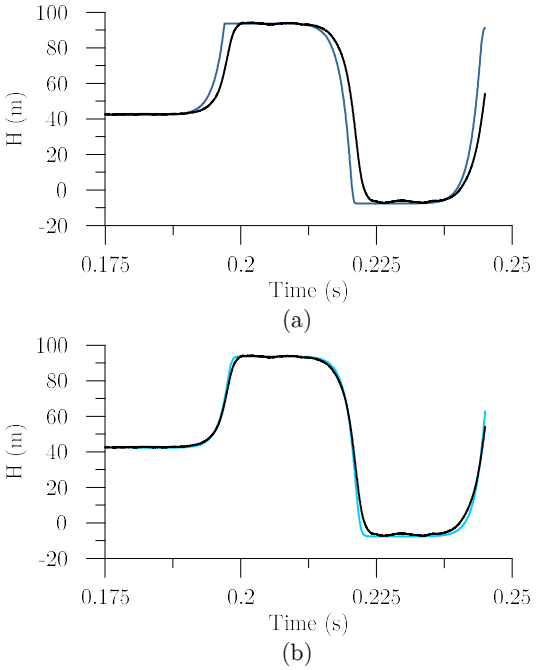

Figure 6. Pressure wave results for: (a) first approach; (b) second approach

5.3. Model validation for turbulent flows

Instantaneous acceleration-based and convolution-based models results are compared with turbulent flow experimental data. Brunone *et al.* (1991) formulation parameters that better fit experimental results are k_3 =0.016 and the relaxation coefficient θ =0. Ramos *et al.* (2004) formulation uses k_x and k_t equal to 0.026 and 0.020, for θ =1. The comparison between both models and experimental results is presented in Figure 7. No numerical instabilities are seen for turning the numerical scheme explicit with θ =0 and a good match is obtained for both models. A slight pressure wave delay is observed in the Brunone *et al.* (1991). Ramos *et al.* (2004) fits much better the pressure damping and pressure wave shift as both acceleration components have a different calibrated coefficient.
Convolution-based models shown in Figure 8 denote a good fitting with experimental data as Reynolds number is small and time between pulses is comparatively small (order of magnitude 10^{-2} s) (Ghidaoui and Mansour, 2002).

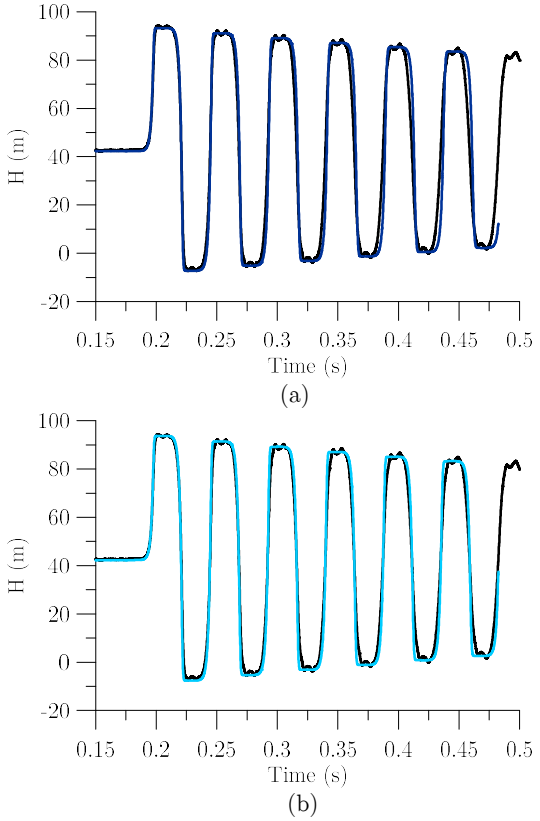

Figure 7. Experimental and numerical model results for Q_0=450 lh^{-1} using: (a) Brunone *et al.*(1991) and (b) Ramos *et al.*(2004).

5.4. Model validation for laminar flows

Comparing instantaneous acceleration-based models results with laminar flow experimental data for the same decay coefficients in Figure 9, pressure damping is reasonably characterized. However, the pressure wave shape is not well described by IAB formulations as viscous forces components are not correctly described by the local acceleration using only the previous time step local and convective accelerations.

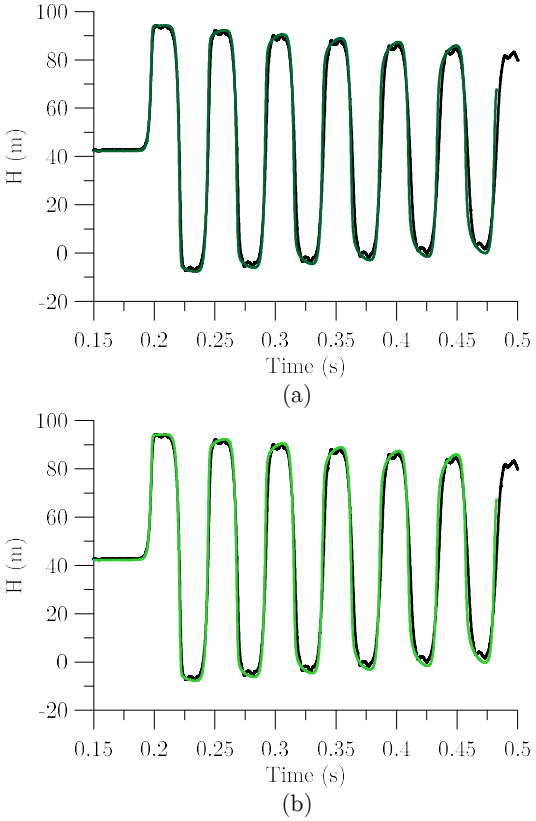

Figure 8. Experimental and numerical model results for Q_0=450 lh-1 using: (a) Zielke (1968) and (b) Vardy et al.(2003).

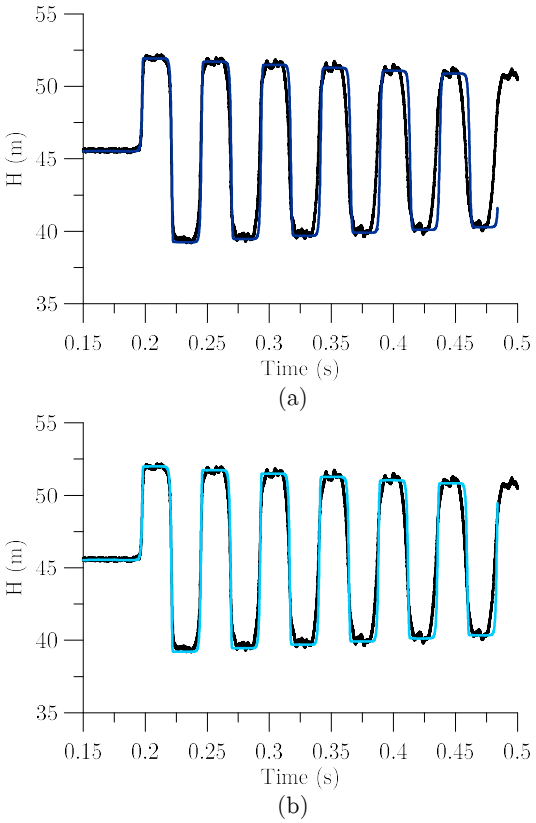

Figure 9. Experimental and numerical model results for Q_0=56.5 lh^{-1} using: (a) Brunone *et al.*(1991) and (b) Ramos *et al.*(2004).

Convolution-based models results are compared with experimental data in Figure 10. These comparisons show good results between experimental data and numerical results both for Zielke (1968) and Vardy and Brown (2003) formulations. The former was theoretically developed and the latter tends to Zielke's solution as Vardy's weighting functions to be the same in laminar conditions. These formulations accurately characterize both the pressure damping in time, as well as the pressure wave shape. However, simulation time strongly increases using these formulations.

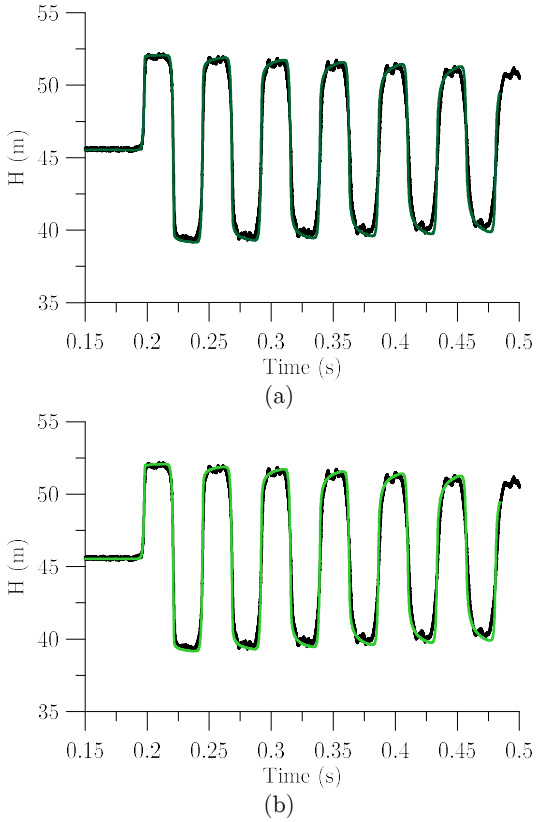

Figure 10. Experimental and numerical model results for Q_0=56.5 lh^{-1} using: (a) Zielke (1968) and (b) Vardy *et al.*(2003).

6. Wall shear stress

In this study, wall shear stress measurements were carried out using a hot-film probe depicted in Figure 11, using a constant temperature anemometry (CTA) operation.

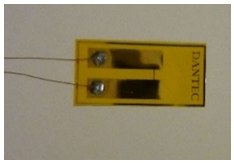

Figure 11. Hot-film probe

As the used methodology is not considered direct (i.e. other physical processes are measured and further treated) a calibration curve is required. First, the MiniCTA is configured for a 28°C flow and a 40°C sensor temperature. MiniCTA output tension is measured for each steady-state flow rate with a 10kHz data acquisition frequency. A relation between measured tension and the theoretical wall shear stress obtained by Blasius formulation is used. Wall shear stress is calculated by:

$$\tau_w = 0.3164\,\mathrm{Re}^{-0.25}\,\gamma\,(U^2/8g) \tag{6.1}$$

in which γ is the water specific weight.

The calibration curve for the carried out tests is presented in Figure 12 with a seven degree polynomial function give by:

$$\begin{aligned}\tau_w &= 0.98V - 17.99V^2 + \\ &135.03V^3 - 484.51V^4 + 930.72V^5 \\ &-875.74V^6 + 321.98V^7\end{aligned} \tag{6.2}$$

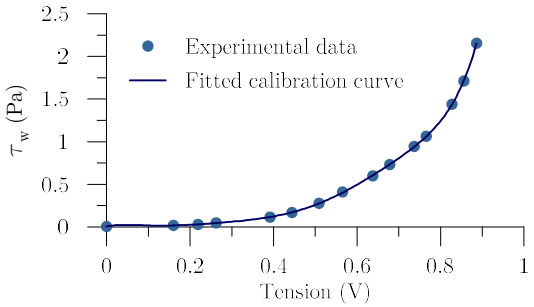

Figure 12. Wall shear stress calibration curve

When comparing wall shear stress measurements with numerical model results for Zielke (1968) formulation with initial steady-state flow rate of 450 and 56.5 lh^{-1} in Figure 13, major discrepancies are observed. These differences can be due to the 1D model development, to the probe not being inside the viscous sub-layer or the thermal inertia/delay of the probe heating.

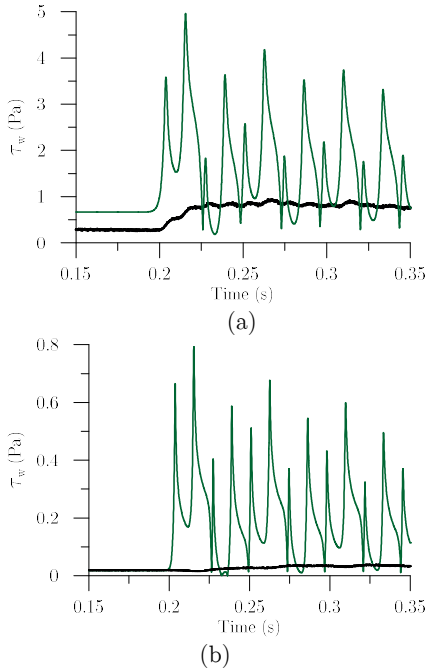

Figure 13. Wall shear stress measurements and Zielke (1968) formulation results for: (a) 450 lh^{-1} and (b) 56.5 lh^{-1} (black – experimental results; green – Zielke's formulation results)

For the proposed valve closure in the 1D model and with the same CFD model, wall shear stress results from each model are compared in Figure 14.

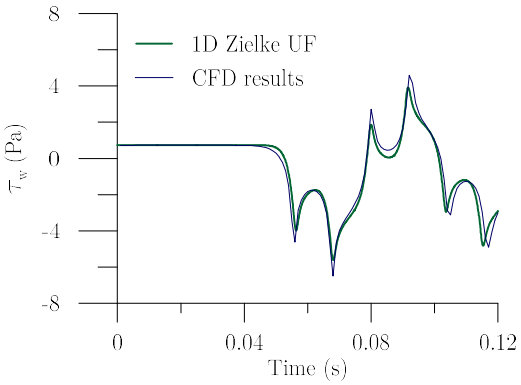

Figure 14. 1D model and CFD wall shear stress results

To assess if the probe is inside the viscous sub-layer, CFD results for 14 steady-state flow rates series are used. Shear stress can be split in two components, viscous and turbulent, which are defined according to:

$$\begin{aligned} \tau(r) &= \tau_v + \tau_t \\ \tau(r) &= -\mu\frac{\partial V}{\partial r} + \rho\overline{u'v'} \end{aligned} \tag{6.3}$$

being τ_v and τ_t the viscous and turbulent components of wall shear stress and u' and v' the fluctuating velocity components, respectively.

According to equation (6.3) the viscous component of shear stress can be estimated based on velocity profiles according to:

$$\tau_v(r_i) \approx -\mu\frac{v_i - v_{i+1}}{r_i - r_{i+1}} \tag{6.4}$$

For each steady-state flow rate, measured shear stress is compared with CFD estimated shear stress and the estimated location is obtained when the shear value is the same. The probe location is further compared with viscous sub-layer thickness given by (Schlichting, 1979, Cardoso, 1998):

$$\delta^* = \frac{11.6\nu}{u^*} \tag{6.5}$$

in which $u^* = \sqrt{(\tau_{ws} \,/\, \rho)}$.

The comparison between the estimated probe location and the viscous sub-layer thickness is depicted in Figure 15.

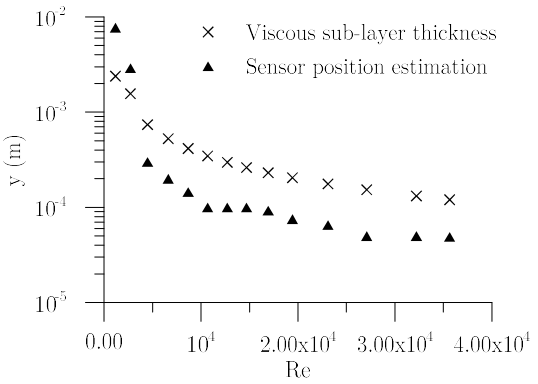

Figure 15. Probe sensor location and viscous sub-layer thickness for each steady-state flows

Excepting for the first two flow rates which are associated with larger errors, the probe is within the viscous sub-layer. For the initial points the probe will be also in the viscous sub-layer as its thickness increases with the flow rate decrease. As such, the hypothesis of the probe not being inside the viscous sub-layer is false and thus, this hypothesis does not explain the measurements discrepancies.

At last, thermal inertia of the heating process is analysed. For each presented initial steady-state flow rates, Zielke (1968) numerical results are subject of moving averages with different amount of intervening past instances during measurements.

The comparison between these results and experimental data for the previous transient is shown in Figure 16. Turbulent results first peak accurately fit for a time delay, t_d, of 2.5 ms (0.0025 s), regardless the following oscillations. These may be due to measuring differences as the sensor is not perfectly aligned with the wall (despite being in the viscous sub-layer). Laminar steady-state flow rate results completely mismatch the results from the moving averages. This can be justified by the lack of points in laminar flow regime for the calibration curve or by the lack of sensitivity of the sensor for such velocities. When converting measured tension to wall shear stress, a slight variation introduces high differences than it should and wall shear stress is underestimated.

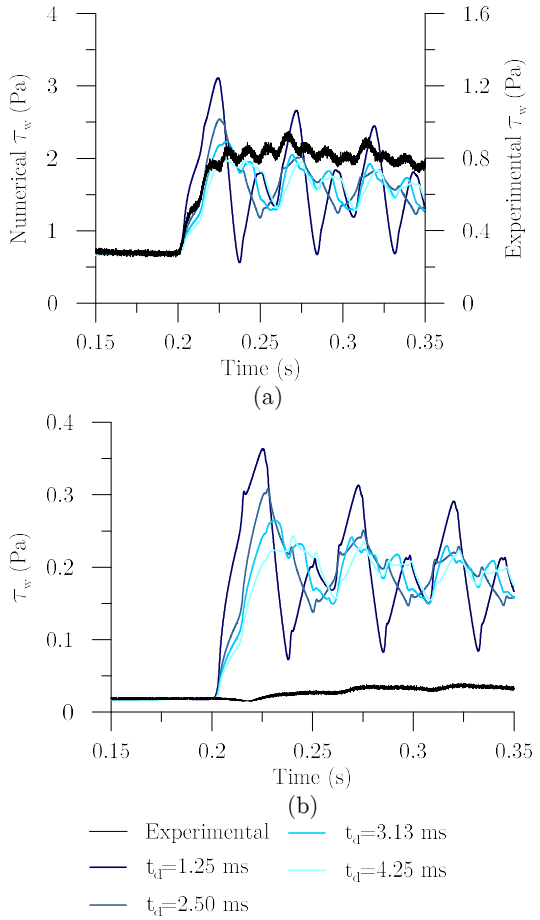

Figure 16. Experimental results with Zielke's (1968) moving average results for different time delays: (a) 450 lh^{-1} and (b) 56.5 lh^{-1}

7. Conclusions

Valve behaviour | Flow rate variation and head loss coefficients for each closure angle, which determines the valve behaviour, are Reynolds number dependent as the viscous forces are predominant in laminar and transitional flows and inertial forces are predominant in turbulent flows (influencing greatly the valve behaviour for closures below 83%). Valve dynamic behaviour is determined using two approaches for different closure times. The first considers the valve as an in-line valve. A flow rate discrepancy between the static and the dynamic behaviour is observed at higher closure angles due to the abrupt manoeuvres. The second approach idealizes a discharge to atmosphere considering only the pressure upstream the valve, which allows neglecting the pipe system at downstream the valve in the numerical model. Spherical valve effective closure time varies between 5 to 10% of the total closure time.

One-dimensional models | A 1D numerical model with different unsteady friction formulations was implemented, calibrated and compared with experimental data from the carried out transient events. A good fitting is obtained for both instantaneous acceleration-based and convolution-based models for turbulent flow measurements. Instantaneous acceleration-based do not accurately describe laminar flow. Convolution-based models describe reasonably well the pressure wave behaviour for all flows.

Wall shear stress | Wall shear stress measurements were carried out using a hot-film probe and constant temperature anemometry (CTA) measurement technique. Collected tension was subject of a calibration stage using the Blasius friction approach. The obtained wall shear stress after calibration was compared with numerical results and major discrepancies were observed in terms of extreme values, phase and shape. Observed discrepancies can be due to: (i) the calibration curve that is highly sensitive to temperature variations and the amount of tested flow rates; (ii) the position of the hot-film in relation to the pipe wall, which was accurately installed in the viscous sub-layer; (iii) the MiniCTA heating frequency response to transient events with a delay of 0.0025 s.

References

Allievi, L. (1902) Theory of Water-Hammer. translated by E. Halmos (1925) Typography Riccardo Garroni.

Berca, E.-L. (2007), Instrumentation development for wall shear-stress applications in 3D complex flows, PhD. Thesis. École Polytechnique Fédérale de Lausanne, Section de génie mécanique.

Bergant, A., Simpson, A. and Vitkovsk, J. (2001) Developments in unsteady pipe flow friction modelling. Journal of Hydraulic Research 39 249-257. DOI 10.1080/00221680109499828.

Brito, M., Sanches, P., Ferreira, R. M. and Covas, D. I. C. (2014) PIV Characterization of Transient Flow in Pipe Coils. Procedia Engineering 89 1358 - 1365. DOI 10.1016/j.proeng.2014.11.458.

Brunone, B. and Berni, A. (2010) Wall shear stress in transient turbulent pipe flow by local velocity measurement. Journal of Hydraulic Engineering 136 716-725. DOI 10.1061/(ASCE)Hy.1943-7900.0000234.

Brunone, B., Golia, U. M. and Greco, M. (1991) Some remarks on the momentum equation for fast transients. in International Meeting on Hydraulic Transients and Water Column Separation, Universidad Politecnica de Valencia.

Cardoso, A. H. (1998) Hidráulica Fluvial, Gulbenkian, F. C. ISBN: 9723108151. Lisboa, Portugal

Chaudhry, M. H. (2014) Applied Hydraulic Transients, ISBN: 978-1-4614-8537-7.

Chaudhry, M. H. and Hussaini, M. Y. (1985) Second-order accurate explicit finite-difference schemes for waterhammer analysis. Journal of Fluids Engineering 107 523-529. DOI 10.1115/1.3242524.

Covas, D. (2003), Inverse transient analysis for leak detetion and calibration of water pipe systems modelling special dynamic effects, PhD. Thesis. Imperial College of Science, Technology and Medicine, Department of Civil and Environmental Engineering.

Ghidaoui, M. S. and Mansour, S. (2002) Efficient treatment of the Vardy-Brown unsteady shear in pipe transients. Journal of Hydraulic Engineering 128 102-112. DOI 10.1061/(ASCE)0733-9429(2002)128:1(102)

Ghidaoui, M. S. and Zhao, M. (2005) A review of water hammer theory and practice. Applied Mechanics Reviews 58 49-76. DOI 10.1115/1.1828050.

Joukowsky, N. (1900) Über den hydraulischen Stoss in Wasserleitungsröhren, Mémoires de l'Académie Impériale des Sciences de St.-Pétersbourg

Lescovich, J. E. (1967) The control of water hammer by automatic valves. American Water Works Association 59 632-644. DOI 41265218

Martins, N. (2016), Transient flow dynamics in pressurized pipes: CFD modelling and experimental analysis, PhD Thesis. Instituto Superior Técnico, DECivil.

Martins, N., Soares, A., Ramos, H. and Covas, D. (2016) CFD modeling of transient flow in pressurized pipes. Computers & Fluids 126 129-140. DOI 10.1016/j.compfluid.2015.12.002.

Michaud, J. (1878) Coups de belier dans les conduites: etude des moyens employes pour en attenuer les effets. 4 55-64, 65-77.

Ramos, H., Almeida, A., Portela, M. and Almeida, H. P. (2000) Guidelines for design of small hydropower plants. WREAN and DED, Belfast, North Ireland

Ramos, H., Covas, D., Borga, A. and Loureiro, D. (2004) Surge damping analysis in pipe systems: modelling and experiments. Journal of Hydraulic Research 42 413-425. DOI 10.1080/00221686.2004.9641209.

Schlichting, H. (1979) Boundary-layer theory, ISBN: 978-3-540-66270-9.

Trikha, A. K. (1975) An Efficient Method for Simulating Frequency-Dependent Friction in Transient Liquid Flow. Journal of Fluids Engineering 97 DOI 10.1115/1.3447224.

Vardy, A. E. and Brown, J. M. B. (2003) Transient turbulent friction in smooth pipe flows. Journal of Sound and Vibration 259 1011-1036. DOI 10.1006/jsvi.2002.5160.

Vardy, A. E., Brown, J. M. B. and Hwang, K.-L. (1993) A weighting function model of transient turbulent pipe friction. J Hydraul Res 31 533-548. DOI 10.1080/00221689309498876.

White, F. M. (2010) A Brief Introduction To Fluid Mechanics, ISBN: 9780470596791.

Zielke, W. (1968) Frequency-dependent friction in transient pipe flow. Journal of basic engineering 90 DOI 10.1115/1.3605049.